Geophysical Journal International

Geophys. J. Int. (2018) **214,** 1191–1205
Advance Access publication 2018 May 10
GJI Geodynamics and tectonics

doi: 10.1093/gji/ggy181

In search of laterally heterogeneous viscosity models of glacial isostatic adjustment with the ICE-6G_C global ice history model

Tanghua Li,[1] Patrick Wu,[1,2] Holger Steffen[3] and Hansheng Wang[4]

[1] *Department of Earth Sciences, University of Hong Kong, Pokfulam Road, Hong Kong. E-mail: ppwu@hku.hk*
[2] *Department of Geoscience, University of Calgary, Calgary, Alberta T2N 1N4, Canada*
[3] *Geodata Division, Lantmäteriet, Lantmäterigatan* 2C, 80182 *Gävle, Sweden*
[4] *State Key Laboratory of Geodesy and Earth's Dynamics, Institute of Geodesy and Geophysics, Chinese Academy of Sciences, Wuhan* 430077*, China*

Accepted 2018 May 3. Received 2018 March 29; in original form 2017 October 23

SUMMARY

Most models of glacial isostatic adjustment (GIA) assume that the Earth is laterally homogeneous. However, seismic and geological observations clearly show that the Earth's mantle is laterally heterogeneous. Previous studies of GIA with lateral heterogeneity mostly focused on its effect or sensitivity on GIA predictions, and it is not clear to what extent can lateral heterogeneity solve the misfits between GIA predictions and observations. Our aim is to search for the best 3-D viscosity models that can simultaneously fit the global relative sea level data, the peak uplift rates (u-dot from the Global Navigation Satellite System) and peak gravity-rate-of-change (g-dot from the Gravity Recovery And Climate Experiment satellite mission) in Laurentia and Fennoscandia. However, the search is dependent on the ice and viscosity model inputs—the latter depends on the background viscosity and the seismic tomography models used. In this paper, the ICE-6G_C ice model, with Bunge and Grand's seismic tomography model and background viscosity models close to VM5 will be assumed. A coupled Laplace-finite element method is used to compute gravitationally self-consistent sea level change with time-dependent coastlines and rotational feedback in addition to changes in deformation, gravity and the state of stress. Several laterally heterogeneous models are found to fit the global sea level data better than laterally homogeneous models. Two of these laterally heterogeneous models also fit the observed peak g-dot and u-dot rates in Laurentia simultaneously. However, even with the introduction of lateral heterogeneity, no model that is able to fit the present-day g-dot and uplift rate data in Fennoscandia has been found. Therefore, either the ice history of ICE-6G_C in Fennoscandia and Barents Sea needs some modifications or the sublithospheric property/non-thermal effect underneath northern Europe must be different from that underneath Laurentia.

Key words: Loading of the Earth; Lateral heterogeneity; Creep d; Sea level change; Crustal deformation; Time variable gravity.

1 INTRODUCTION

Glacial isostatic adjustment (GIA) describes the dynamic response of the Earth to surface ice and water load redistribution during glacial cycles of an ice age. GIA models have two inputs: the ice glaciation–deglaciation history and the viscoelastic structure of the Earth. The outputs include the history of Earth's various responses to GIA such as surface motion, surface mass distribution, changes in geoid, gravity, stresses, moments of inertia, etc. Using models of GIA and the constraints provided by GIA observations [e.g. relative sea level (RSL) data, land uplift rates from Global Navigation Satellite System (GNSS) data, observations of gravity-rate-of-change and Earth's anomalous rotational motion, etc.], models of ice sheet thickness history (Peltier 2004; Lambeck *et al.* 2014) and radial structure of mantle viscosity have been inferred (Mitrovica & Forte 1997; Lambeck & Johnston 1998; Peltier 1998; Kaufmann & Lambeck 2000). Recently, the global ICE-6G_C ice history model has been developed (Argus *et al.* 2014; Peltier *et al.* 2015) in combination with viscosity models VM5a, VM5b and VM6 (Engelhart *et al.* 2011; Roy & Peltier 2015; Hawkes *et al.* 2016).

In the development of the above ice models, the earth models are always assumed to be laterally homogeneous. However, surface geology and seismic tomography clearly show that material properties inside the Earth vary not only radially, but also laterally (Ekström & Dziewonski 1998; Bunge & Grand 2000). In fact, based on GIA modelling, Engelhart *et al.* (2011) found that while VM5b

can resolve a lot of misfits in the RSL data, some in the northern Atlantic region apparently 'require laterally heterogeneous viscosity models'.

Actually, the study of lateral heterogeneity in GIA began in the 1980s and has become more mature recently. Early investigations of GIA with lateral heterogeneity were based on axisymmetric ice and simple laterally heterogeneous flat-Earth models. They found that lateral heterogeneities have a strong effect on GIA observations, but the amplitude of the effect varies with location from the ice sheet centre and also depends on the type of GIA measurements used (Sabadini *et al.* 1986; Gasperini & Sabadini 1989; Sabadini & Gasperini 1989; Gasperini *et al.* 1991; Giunchi *et al.* 1997; Kaufmann *et al.* 1997).

Later, more realistic 3-D flat-earth models with lateral heterogeneities deduced from geologic and geophysical data (including seismic tomography) were studied together with more realistic regional ice models (Kaufmann & Wu 1998, 2002; Kaufmann *et al.* 2000, 2005; Wu 2005; Steffen *et al.* 2006; Schotman *et al.* 2008, 2009). They confirmed earlier findings with 2-D models and showed that lateral heterogeneities can significantly affect the amplitude and pattern of land uplift, geoid height and gravity anomaly around the centre of rebound, but its effect on horizontal motion is much larger, and the pattern of horizontal velocity can be quite different from that predicted by laterally homogeneous models. With these more realistic GIA models, Kaufmann & Wu (2002) showed that 3-D mantle structures cannot be properly resolved with 1-D Earth models. In addition, the effects of lateral heterogeneity of individual depth layers on surface uplift rate and horizontal velocities were studied by Wu (2005).

Wu (2002) coupled a spherical finite element grid with the Laplace equation to study GIA on a spherical, self-gravitating incompressible Earth with lateral heterogeneity and demonstrated the importance of mode coupling in the presence of lateral heterogeneity or nonlinear rheology. Zhong *et al.* (2003) also developed a 3-D spherical incompressible Earth model and studied the effects of lateral lithospheric thickness variation on relative change in sea level, but no comparison with RSL data was shown. Latychev *et al.* (2005a,b) developed a 3-D spherical compressible Earth model and confirmed that lateral viscosity variations have a larger effect on horizontal velocities than on uplift rates. Whitehouse *et al.* (2006) used the model of Latychev *et al.* (2005b) to study the effects of lateral heterogeneity on uplift rate and horizontal velocities in Fennoscandia. Similarly, Martinec & Wolf (2005) used an axisymmetric spherical model to study the effect of a thick craton on the relaxation time spectrum in Fennoscandia. Tanaka *et al.* (2011) used the spectral-finite element method to compute deformation in a compressible, self-gravitating Earth to study the effects of compressibility on vertical and horizontal motion. The above studies did not solve the gravitationally self-consistent sea level equation because they mainly focused on the effects of lateral heterogeneity on uplift rate and horizontal velocities. Spada *et al.* (2006) studied the effects of lateral heterogeneities on RSL for a spherical non-self-gravitating Earth, and the sea level equation was not solved either.

Sea level equation for self-gravitating oceans was later included in 3-D GIA models (Wu & van der Wal 2003; Wu 2004; Wu *et al.* 2005; Wang & Wu 2006a,b; Wang *et al.* 2011). Paulson *et al.* (2005) included rotational feedback in the sea level equation and studied the effects of lateral heterogeneities deduced from a seismic tomography model on an incompressible Earth, but no comparison with RSL or other data was shown. A *et al.* (2012) included compressibility in the model of Paulson *et al.* (2005) and studied the effect of compressibility on uplift rate in Antarctica. They concluded that a 3-D structure complicates the interpretation of GPS data using a 1-D GIA model, and that confirms the finding of Kaufmann & Wu (2002).

With the improvements of 3-D GIA earth models (e.g. including self-gravity, sea level equation, compressibility, etc.), sensitivity kernels that include the effects of lateral heterogeneity have also been computed (Wu 2006; Steffen *et al.* 2007; Steffen & Wu 2014). They were used to search for optimal locations of GIA data that can better constrain lateral heterogeneities (Wu *et al.* 2010; Steffen *et al.* 2012, 2014b).

It is important to note that most works mentioned so far are mainly interested in studying the effects of lateral heterogeneity or its sensitivity. Only a few studies actually show the comparison between predictions of lateral heterogeneous GIA models with observations. Even in these few studies, there was no serious effort to harmonize lateral heterogeneous GIA models with the global RSL data, the crustal velocities from GNSS or g-dot measurements from land or space missions simultaneously. Thus, it is not clear how far the introduction of lateral heterogeneity can solve the misfits between GIA predictions and observations. It turns out that a realistic model of lateral viscosity variation and thus a better 3-D viscosity model is the first step to achieve this aim.

As mentioned above, the model of lateral heterogeneity has also improved. In the early days, lateral heterogeneity was deduced qualitatively from geologic and geophysical data (e.g. Kaufmann *et al.* 2000). Later lateral viscosity variations were deduced quantitatively from seismic tomography models (e.g. Kaufmann *et al.* 2005; Paulson *et al.* 2005; Steffen *et al.* 2006; Wang & Wu 2006b; Whitehouse *et al.* 2006; Wang *et al.* 2008) by using a scaling relationship (e.g. Ivins & Sammis 1995) which assumes that the origin of the seismic wave anomalies in tomography models are completely due to thermal expansion (i.e. anharmonicity). However, Wang *et al.* (2008) found that such scaling relationship may overcorrect the misfits between the predictions of laterally homogeneous models and the GIA observations. If the scaling relation is multiplied by a factor β (with value between 0 and 1), then the predictions of the lateral heterogeneity model are able to better fit the observations. Since seismic anomalies in a tomography model can have contributions from thermal, chemical or non-isotropic pre-stress effects, Wang *et al.* (2008) argued that the factor β represents the contribution of thermal effects on lateral heterogeneity. Another issue pointed out by Karato (2008) is that the effect of anelasticity is also important and must be included in the scaling relationship. Thus, Wu *et al.* (2013) included both the effects of anharmonicity and anelasticity in the scaling relation between seismic velocity variations and lateral viscosity variations. In addition, they allowed the value of β in the upper mantle (β_{UM}) to be different from that in the lower mantle (β_{LM}), and searched the combination (β_{UM}, β_{LM}) that can give the best fit to global RSL data, peak uplift rates and peak g-dot in Laurentia and Fennoscandia simultaneously. They interpreted the combination of β in the upper and lower mantle as the contributions of thermal effects on seismic anomalies in the upper and lower mantle, respectively. However, ICE-4G was used in Wu *et al.* (2013), and that model has been shown to have some serious limitations (e.g. the ice thickness in western Canada was too thin). With the recent development of new global ice models, it is time to update the work of Wu *et al.* (2013).

Thus, the aim of this paper is to search for the best laterally heterogeneous viscosity model with an assumed ice history and background viscosity model that is able to fit the global RSL data,

the GIA uplift rate (u-dot) signals (from GNSS) and also the gravity-rate-of-change (or g-dot) signals from the Gravity Recovery And Climate Experiment (GRACE) satellite mission over the centres of rebound in Laurentia and Fennoscandia simultaneously. In this study, we focus on the ICE-6G_C-VM5 combination as the ice history model is the only freely available global ice history model to date. Clearly, this ice model is not perfect, especially in Antarctica where the ice history is poorly known. The same may also be true in Greenland and in other places. In fact, the results of this study strongly suggest that the ice thickness history in Fennoscandia and the Barents Sea needs modifications, although the ice history in North America is more consistent with the observational data.

Note that with the ICE-6G_C model as the fixed input of our GIA model, the aim of fitting the g-dot and u-dot data in Laurentia and Fennoscandia must be slightly qualified. This is because previous studies have shown that the patterns of u-dot and g-dot (including the location of the peaks) are determined mostly by the ice model while the amplitudes of u-dot and g-dot are determined mostly by the viscosity structure of the mantle (Wang & Wu 2006a,b). With the ice model fixed, it may not be possible to fit the observed patterns of u-dot and g-dot by varying the lateral viscosity structure. Thus, our focus will be on finding 3-D mantle viscosity models that can give the best fit to the global RSL data and the peak amplitudes of u-dot and g-dot near the centres of GIA in Laurentia and Fennoscandia simultaneously.

The 3-D viscosity variation is assumed to be the superposition of radial and lateral viscosity structures logarithmically (Wang & Wu 2006c; Wang *et al.* 2008). The radial background structure generally consists of an elastic lithospheric layer on top of at least two mantle layers (upper and lower mantle) subdivided by 660 km depth. The thickness of the lithosphere as well as the number and the viscosity of mantle layers can be investigated, which however means that the number of background models to test can easily be a few hundred or thousand. Therefore, as a start, we limit our model space in this study to the corresponding earth structure VM5a of ICE-6G_C but also investigate a selection of other radial background viscosity models with minor variations from VM5a or VM5b. The viscosity profiles of these and the background viscosity of two of our best models are listed in Appendix C.

To quantify lateral viscosity variations, we apply Bunge and Grand's seismic tomography model (Bunge & Grand 2000), which is different from the S20A (Ekström & Dziewonski 1998) model used in Wu *et al.* (2013). It also has a higher spatial resolution than S20A. Again, investigation of the effects of different seismic tomography models on GIA predictions is challenged by the number of models one can compute, therefore we start with just this one. However, we have performed a small test in Appendix B, which shows that the results reported here do not significantly depend on the choice between these two seismic tomography models.

In the next two sections, we describe the details of the observational data used and our modelling approach. We would like to point to the fact that compared to Wu *et al.* (2013), we have used an expanded RSL data set and updated GIA g-dot maps and that our finite element grid has a higher spatial resolution of $0.5^\circ \times 0.5^\circ$ instead of the $2^\circ \times 2^\circ$ grid used in Wu *et al.* (2013). Moreover, time-dependent coastlines and rotational feedback have been included in the sea level computation. We then present and discuss our results in Section 4, followed by the conclusions in Section 5.

2 GIA OBSERVATIONAL DATA

Our observational data include: (i) global RSL data, (ii) land uplift rates (or u-dot) from GNSS stations in Laurentia and Fennoscandia, (iii) the gravity-rate-of-change (g-dot) in these regions observed by GRACE. RSL data are important because they record the land uplift and gravity field change history during the last several thousands of years. U-dots from GNSS data and g-dot data are independent measurements of the current rate-of-change. Although empirical relations between them have been proposed (Wahr *et al.* 1995), the empirical relation is found to have some dependence on location (Lambert *et al.* 2013) and ice sheet size (Olsson *et al.* 2015). Furthermore, u-dot data from GNSS are sparser than g-dot data from GRACE.

Note that GNSS and GRACE data not only have contributions from GIA alone, but also measure the deformation from other geological processes. For example, the GNSS data used for GIA studies must have the tectonic, recent melting and hydrological components removed. Similarly, recent hydrology contributions must also be removed from the GRACE data. In the past, the hydrology signal was obtained from models of hydrology or indirectly from GIA models. However, these models are far from perfect and so the estimated hydrology signal may not be reliable. A better approach is to estimate the hydrology signal and recent melting directly from observational data (Wang *et al.* 2013, 2015). Because of this, the g-dot data are more closely tied with u-dot data from GNSS, although their values are actually not the same even after transformation with the empirical relation. Our values of g-dot are obtained from Wang *et al.* (2015). The peak uplift rates due to GIA are around

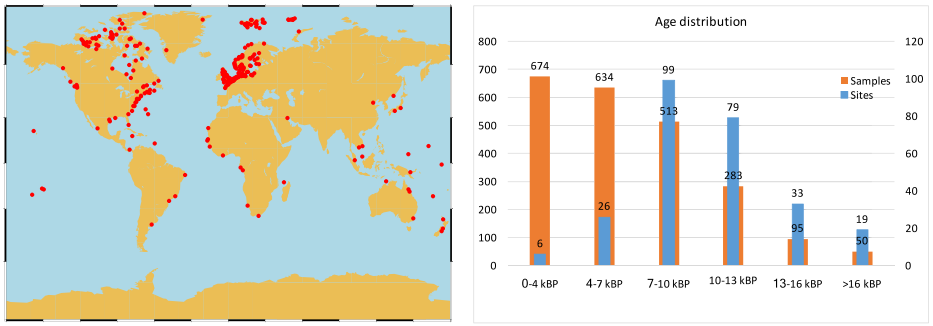

(a) (b)

Figure 1. Overview of the location of RSL data used in this study (a). The red dots represent the locations of the RSL sites with long-time record. Age distribution of 2249 data samples (the orange bars) and the oldest beach in each of the 262 RSL sites (the blue bars) (b).

12.5 ± 1.5 mm yr^{-1} in Laurentia (Wang *et al.* 2015; Simon *et al.* 2016) and 10.20 ± 1 mm yr^{-1} in Fennoscandia (Kierulf *et al.* 2014). The g-dot rates from GRACE after the removal of the contribution of hydrology are 1.8 ± 0.2 μGal yr^{-1} in Laurentia and 1.35 ± 0.2 μGal yr^{-1} for Fennoscandia (Wang *et al.* 2015).

Our RSL database is based on the University of Toronto collection but supplemented and updated with more recent data collected from the literature (Kaufmann & Wolf 1996; Lambeck *et al.* 1998; Dyke *et al.* 2002; Lambeck *et al.* 2014; Steffen *et al.* 2014a). From the RSL database, we selected 262 RSL sites with long time records (spanning more than 3 ka). This subset contains a total of 2249 data samples and their spatial distribution is shown in Fig. 1(a) as red dots. The age distribution of the data samples is visualized by the orange vertical bars in Fig. 1(b). For example, out of the 2249 data samples, there are 634 samples with a sidereal age between 4 and 7 kBP. The blue vertical bars in Fig. 1(b) show the age distribution of the oldest beach in each of the 262 RSL sites. For example, there are 99 sites whose oldest beach has a sidereal age between 7 and 10 kBP. More than 87 per cent of our RSL sites have samples that can date back to 7 kBP or older.

3 GIA MODELLING

The GIA response of a spherical, self-gravitating, materially compressible Maxwell earth is computed using the coupled Laplace-finite element method (Wu 2004). The effects of rotational feedback, time-dependent ocean margin, as well as the effects of sea water entering Hudson Bay and Gulf of Bothnia at the end of deglaciation are also taken into account in the computation of the sea level equation. The finite element grid has $0.5^\circ \times 0.5^\circ$ spatial resolution at the surface but decreases with depth in order to speed up the calculation and minimize memory demand. The lithosphere contains a 60 km thick elastic part underlain by a 40 km thick viscoelastic part (same as in VM5a). In the sublithospheric mantle, layers of elements are grouped together to form four layers: UM1, UM2, LM1 and LM2 which have depth ranges of 100–400, 400–670, 670–1271 and 1271–2891 km, respectively.

Proxy climate data show that the period of a glacial cycle is about 100 ka with a long glacial phase of about 80 ka. We therefore added a linear glacial phase to the ICE-6G_C ice model starting at 108 kBP and reaching glacial maximum around 26 kBP. This ice model will be used with several background radial viscosity models similar to VM5a (see Appendix C). We started with this background viscosity model because the ICE-6G_C and VM5a/VM5b/VM6 combination has been shown to be able to give reasonable fits to many RSL data globally (Engelhart *et al.* 2011; Roy & Peltier 2015; Hawkes *et al.* 2016).

Lateral viscosity perturbations ($\Delta\eta$) in the mantle are derived from the lateral shear velocity anomalies $\left(\frac{\delta v_s}{v_s}\right)$ in Bunge and Grand's seismic tomography model (Bunge & Grand 2000) by employing the scaling relationship (Wu *et al.* 2013; Karato 2008)

$$\log_{10}(\Delta\eta) = \frac{-0.4343}{[\partial \ln v_s/\partial T]_{\mathrm{ah+an}}} \frac{(E^* + pV^*)}{RT_0^2} \frac{\delta v_s}{v_s} \beta,$$

where $E*$, $V*$, p, R and T_0 are the activation energy, activation volume, pressure, gas constant and background temperature profile, respectively. Here, $[\partial \ln v_s/\partial T]_{\mathrm{ah+an}}$ includes both the effects of anharmonicity(ah) and anelasticity(an). The values of the above parameters are given in Karato (2008). The unknown parameter β represents the fractional contribution of the thermal effect on seismic anomalies, and non-thermal effects such as composition and non-isotropic pre-stress effects will consequently have the fractional contribution $1-\beta$.

The lateral viscosity variations with $\beta = 1$ at the four depth ranges UM1, UM2, LM1 and LM2 are illustrated in Fig. 2. To simplify the search in this preliminary study, we assume that the β value in UM1 and UM2 are the same (β_{UM}). Similarly for the β value in LM1 and LM2 (β_{LM}).

Hence, given the background viscosity model, the seismic tomography model and the values of (β_{UM}, β_{LM}), the 3-D viscosity model is completely determined.

4 RESULTS

4.1 Best solution (β_{UM}, β_{LM}) search

In this section, the (β_{UM}, β_{LM}) parameter space will be searched to find the model with the best fit to all three GIA observations simultaneously. In order to quantify the misfit between predictions and observations in RSL, the χ-statistics is calculated. Following Wu *et al.* (2013), we apply $\chi = \sqrt{\frac{1}{N}\sum_{i=1}^{N}\left[\frac{o_i - p_i(m_j)}{\Delta o_i}\right]^2}$, where N represents the number of data, o_i indicates i th observation with uncertainty Δo_i, and $p_i(m_j)$ are the i th prediction for model m_j. Suppose we found the best model m_{b} which has the smallest χ value, then we use the best model to assess the confidence parameter $\psi = \sqrt{\frac{1}{N}\sum_{i=1}^{N}\left[\frac{p_i(m_b) - p_i(m_j)}{\Delta o_i}\right]^2}$ to study the relative fit of the predictions of the other models. For example, models with $\psi \leq 1$ means that they can fit the observations as well as the best model m_{b} within the 1σ-uncertainty. The assumption here is that the observational uncertainties are normally distributed and uncorrelated.

4.2 VM5a as background viscosity model

In Fig. 3(a), the χ statistics for all 262 RSL sites and all models with different β combinations are shown. First we calculate at 0.2 interval of β, then decrease to 0.05 interval to find the best (β_{UM}, β_{LM}) combination. The best model with the least χ value of 3.573 has a β_{UM} value near 0 and β_{LM} around 0.6 (see the red diamonds in Fig. 3). Note that the parameter space with confidence parameter $\psi \leq 1$ (the green and gold areas) lies within the region $\beta_{\mathrm{UM}} < 0.1$ and $\beta_{\mathrm{LM}} < 0.9$, while the area with $\psi \leq 0.5$ (the gold area) is much smaller, with β_{LM} between 0.5 and 0.8 and $\beta_{\mathrm{UM}} < 0.05$. Inspection of the contours reveals that they are almost horizontal which means that the global RSL data cannot resolve the β_{LM} value very well.

Study of the data sensitivity shows that most RSL sites outside the Hudson Bay area have a rather low sensitivity to viscosity in the lower mantle, and only RSL sites in and around Hudson Bay can clearly resolve the viscosity in the lower mantle (see Appendix A, especially Figs A1 and A2, also discussion in Wu *et al.* 2013). Can the inclusion of RSL data outside of Hudson Bay in Fig. 3(a) affect the outcome? To explore this, we show in Fig. 3(b) the χ statistics of RSL data around Hudson Bay only. Although the contour lines are less horizontal, the results are not significantly changed: The best model now has the χ value of 2.707 with $\beta_{\mathrm{UM}} = 0$ and $\beta_{\mathrm{LM}} = 0.6$, while the regions within 1σ uncertainty or 0.5σ extend further away than before. Therefore, based on ICE-6G_C with background model VM5a, the best laterally heterogeneous model has β_{UM} of 0 and β_{LM} of 0.6.

As seen from Fig. 3, RSL data alone cannot constrain lateral heterogeneity very well, therefore a joint inversion with u-dot and

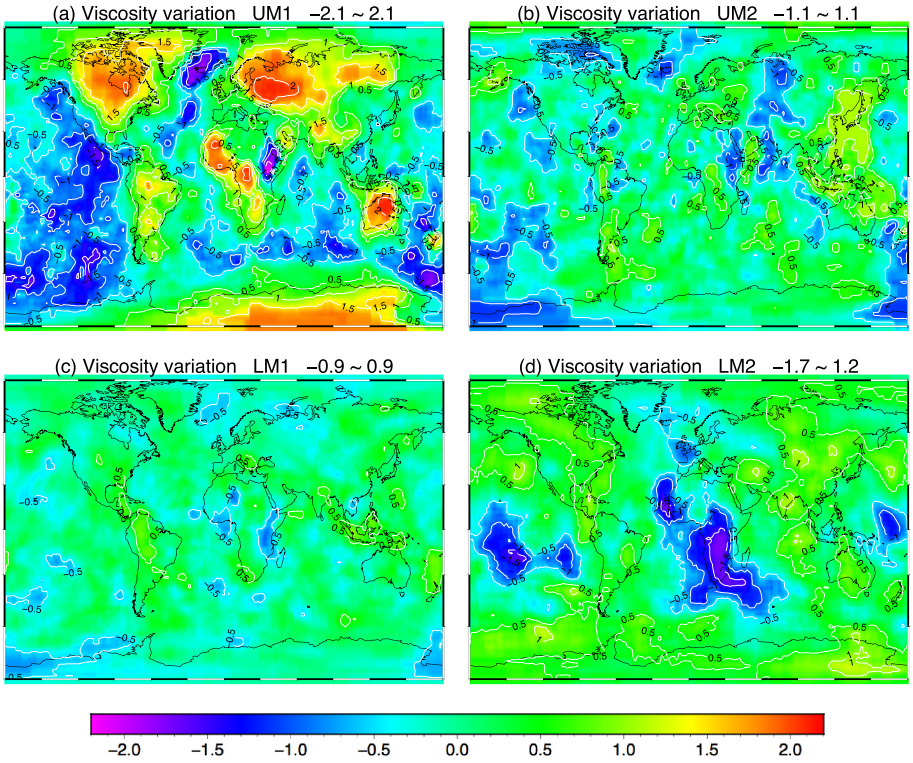

Figure 2. (a–d) Map showing $\log_{10}$ of the lateral viscosity perturbation (units: Pa s) at four depth ranges in the mantle when $\beta = 1$. Here UM1, UM2, LM1 and LM2 have depth ranges of 100–400, 400–670, 670–1271 and 1271–2891 km, respectively. The minimum and maximum values in $\log_{10}$ of the mantle viscosity are also given above each map.

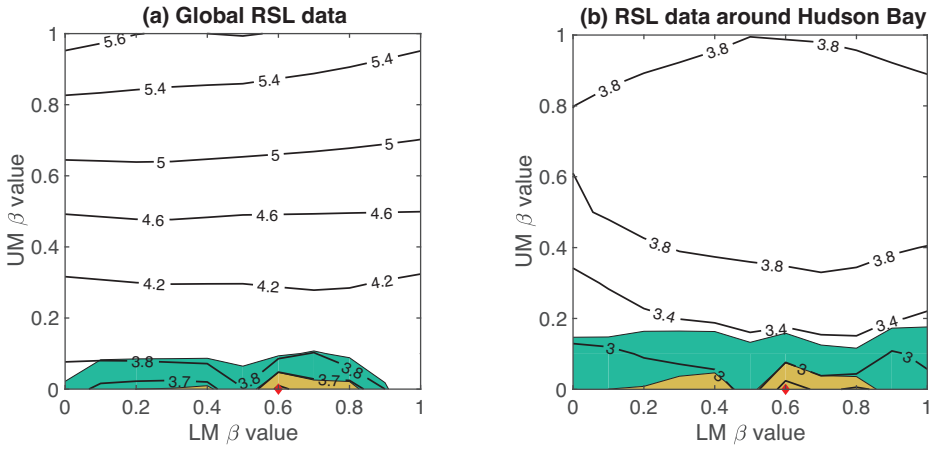

Figure 3. Contour plots of χ for model ICE-6G_C (VM5a) when (a), all 262 RSL sites with long record length and (b), only RSL sites around Hudson Bay are used. Superimposed are the best solution (the red diamond) and the confidence regions with $\psi \leq 0.5$ (the gold region) and $\psi \leq 1$ (the green area).

g-dot is required. Fig. 4 shows the peak values of g-dot and u-dot in Laurentia and Fennoscandia as predicted by various laterally heterogeneous viscosity models ($\beta_{\rm UM}$, $\beta_{\rm LM}$). The red diamond represents the best χ solution for RSL data in Fig. 3.

Figs 4(a) and (b) show that the peak values of g-dot and u-dot in Laurentia increase dramatically with the increase of the $\beta_{\rm LM}$. The predicted peak values can rise as large as 0.64 μGal yr^{-1} for g-dot and 3.95 mm yr^{-1} for u-dot, and they are large enough to be detected by GRACE and GNSS data. However, in Fennoscandia (see Figs 4c and d), the predicted peak values of g-dot and u-dot decrease slightly with the growth in the value of $\beta_{\rm LM}$, especially when $\beta_{\rm UM}$ is larger than around 0.3. This is because the lateral viscosity perturbation in the lower mantle is positive in Laurentia but negative in Fennoscandia, which leads to opposite effects. Besides, as shown in Fig. A1, only the data in Laurentia can 'see' into the lower mantle, and that explains why the variation of magnitudes in Laurentia is notably larger than that in Fennoscandia.

On the other hand, with the increase of the $\beta_{\rm UM}$, the g-dot and u-dot first increase and then decrease significantly, and this is true for both Laurentia and Fennoscandia. The turning point is around $\beta_{\rm UM}$= 0.3. This is because both the lateral viscosity perturbations in UM1 under Laurentia and Fennoscandia are large and positive (Fig.2a), so even though the lateral viscosity perturbations in UM2 under Laurentia are only slightly negative, the overall upper-mantle

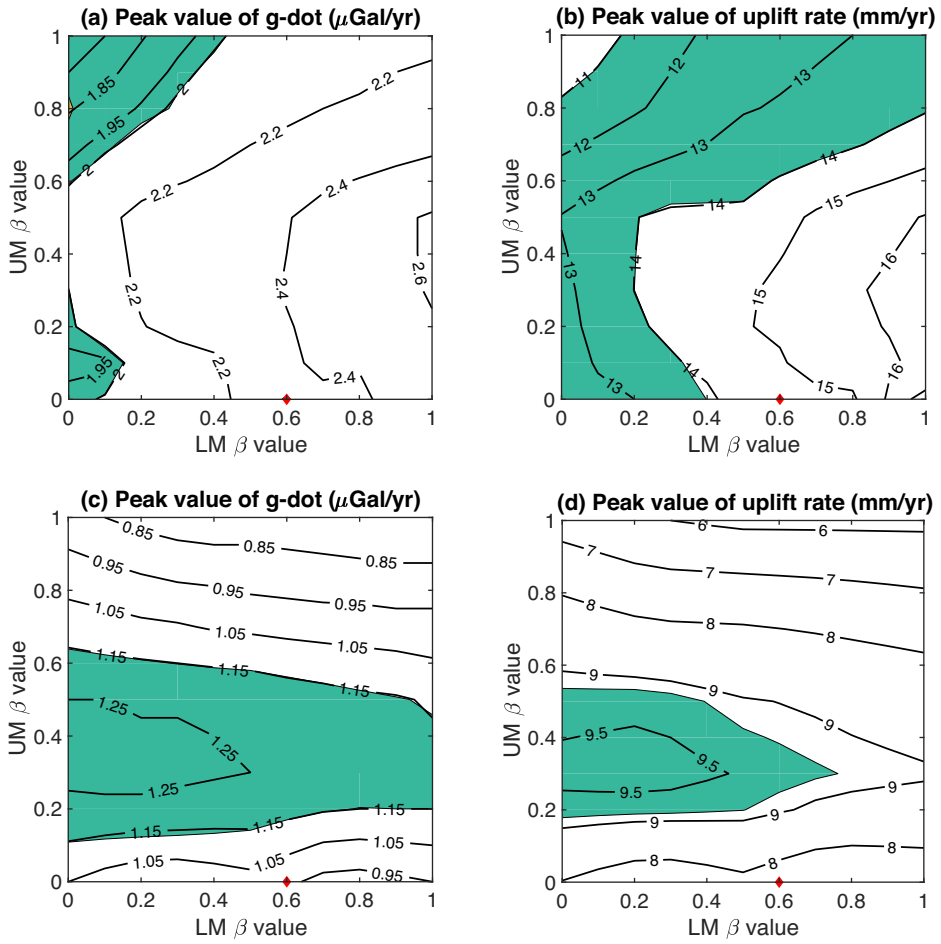

Figure 4. Peak value of g-dot in (a) Laurentia and (c) Fennoscandia; peak value of u-dot in (b) Laurentia and (d) Fennoscandia. The red diamond indicates the best χ statistics in Fig. 3. The values within the observational error bar are coloured in green.

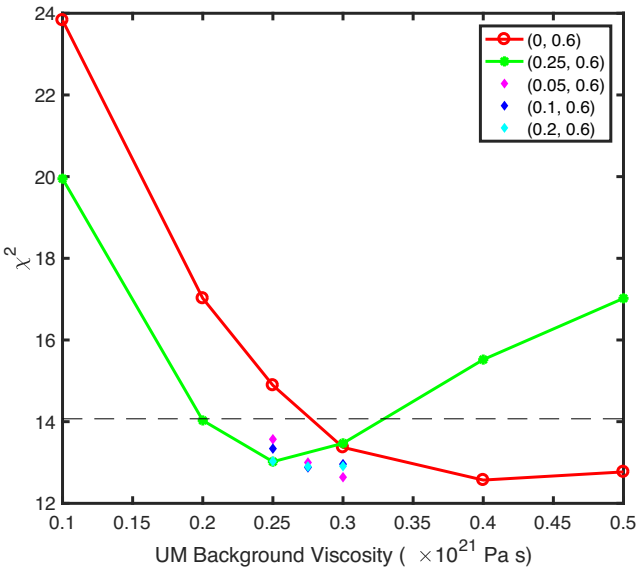

Figure 5. χ-square statistics for the RSLs at 262 sites for different upper-mantle background viscosities with various β_{UM} values. The legend represents (β_{UM}, β_{LM}). The horizontal grey dashed line indicates the χ-square value for the laterally homogeneous ICE-6G_C (VM5a) model.

viscosity still increases with the growth of β_{UM}. Furthermore, different upper-mantle viscosity profiles can get identical present rates (Wu & van der Wal 2003; Argus *et al.* 2014), which has been demonstrated in fig. 4 of Argus *et al.* (2014).

For a combined interpretation of all three GIA observations, it can be seen that the predicted peak values of g-dot and u-dot for our best model in RSL (diamond in Fig. 4) are larger than the observed rates in Laurentia but smaller than the observed rates in Fennoscandia. Thus, the ICE-6G_C (VM5a) combination, although quite successful in fitting a lot of RSL data, fails to fit g-dot and u-dot simultaneously even with the introduction of lateral heterogeneity.

That the results above are not dependent on the choice of the seismic tomography model is demonstrated in Appendix B, where we repeat the above computations using viscosity models converted from the seismic tomography model S20A (Ekström & Dziewonski 1998) instead of Bunge and Grand's model.

In summary, the above confirms that the best β_{UM} value for RSL is 0, which means the upper mantle is laterally homogeneous—this is despite the fact that RSL data are very sensitive to lateral heterogeneity in the upper mantle (see Figs A1a, b and A2a, c, e and f). The problem might be that the background viscosity in the upper mantle is already so high that no lateral viscosity perturbation is permitted. Adding a positive viscosity perturbation to that will naturally decrease the fit to observational data (see Figs 3a and b). This point will be followed up in the next section.

4.3 Other background viscosity models

In view of the fact that VM5a can give a reasonable fit to global RSL data but not the peak g-dot nor u-dot in Laurentia and Fennoscandia, even with lateral heterogeneity, implies that VM5a may not be the best background viscosity model. There are reasons to support that: First, both VM5b (Engelhart *et al.* 2011) and VM6 (Roy & Peltier 2015) models have smaller upper-mantle viscosities than VM5a. In addition, the Fennoscandian relaxation spectrum in Lau *et al.* (2016) prefers an upper-mantle viscosity to be around 0.3×10^{21} Pa s. Because the background viscosity model has a strong impact on the laterally heterogeneous GIA study, especially for the magnitude of u-dot (Wang & Wu 2006c), therefore our next step is to test several background viscosity models with smaller upper-mantle viscosity varied from 0.1×10^{21} to 0.5×10^{21} Pa s (VM5a upper-mantle viscosity) at every 0.1×10^{21} Pa s interval, as well as at 0.25×10^{21} Pa s, which is the upper-mantle viscosity of VM5b model (Engelhart *et al.* 2011). The lower-mantle background viscosity will be the same as that in VM5a, and β_{LM} will be kept at 0.6 since that gives the best RSL χ statistics for both global RSL sites and sites around Hudson Bay only (see Fig. 3).

For these background viscosity models with smaller upper-mantle viscosity, we test several values of β_{UM} between 0 and 0.25. The χ-square statistics for RSL at all 262 sites are plotted in Fig. 5. The horizontal dashed line indicates the value of χ-square for the laterally homogeneous model VM5a, so, models with χ-square below the dashed line give a better overall match with RSL observations than the laterally homogeneous model VM5a. The red line represents $\beta_{UM} = 0$ while the green line is for $\beta_{UM} = 0.25$. As the background viscosity in the upper mantle decreases, their χ-square value for both lines first decrease and then increase. For the red curve, with $\beta_{UM} =$ zero, the minimum is around 0.4×10^{21} Pa s. As the value of β_{UM} increases to 0.25 (the green curve), the minimum moves to about 0.25×10^{21} Pa s. For intermediate values of β_{UM} between 0 and 0.25, their minimum χ-square values also lies around 0.3×10^{21} Pa s.

From the model predictions that we have tested, several background viscosities are found to fit the data for g-dot and u-dot in Laurentia: they are 0.2×10^{21}, 0.25×10^{21}, 0.275×10^{21} and 0.3×10^{21} Pa s. However, the RSL χ for the model with 0.2×10^{21} Pa s is slightly larger than that for VM5a, so we neglect it. For these background viscosity models, we have also tested values of β_{UM} at 0.05 (the magenta diamond in Fig. 5), 0.1 (the blue diamond), 0.2 (the cyan diamond) and 0.25 (the green dot).

The model predicted peak values of g-dot and u-dot in Laurentia and Fennoscandia, as well as χ values for RSL are listed in Table 1. In the first column of Table 1, 'X - (β_{UM}, β_{LM})' is the short name of the viscosity model. Here X times 10^{21} Pa s gives the background viscosity in UM and (β_{UM}, β_{LM}) represent the scaling factors to give lateral viscosity variations in the upper and lower mantle, respectively. As mentioned above, the lower-mantle background viscosity will be the same as that in VM5a. Table 1 shows that when the background viscosity equals 0.275×10^{21} or 0.3×10^{21} Pa s and β_{UM} equals 0.05 or 0.1, the predicted g-dot and u-dot in Laurentia fall within the error bars of the observed data and the RSL χ values are smaller than those for VM5a.

In Fig. 6, the χ statistics of RSL, g-dot and u-dot of two best 3-D models are compared with those for VM5a, VM5b and the best laterally heterogeneous model in Fig. 3. The model 0.3-(0.05, 0.6) gives the best χ statistics for RSL but not the best χ statistics in g-dot and u-dot in Laurentia. However, model 0.275-(0.05, 0.6) gives the best fits to g-dot and u-dot data in Laurentia but not the best χ statistics for RSL.

In order to inspect how the best laterally heterogeneous models are able to fit the observed RSL data compared to VM5a, VM5b and the best laterally heterogeneous model in Fig. 3, we choose the comparison at 16 representative sites in the near field around Laurentia and Fennoscandia, in the intermediate field and also in the far field. The locations of these sites are plotted in Fig. 7. Comparison of RSL predictions with observations are shown in Fig. 8, where the red cross with double error bars are the observed RSL data, the blue dashed lines are predictions of (0.5-(0, 0)), that is, the laterally homogeneous model VM5a, the green dashed lines are for (0.25-(0, 0)) or VM5b, magenta solid lines are predictions of 0.5-(0, 0.6), that is, the best model in Fig. 3, while the black dashed lines and cyan dashed lines are for the best laterally heterogeneous models (0.275-(0.05, 0.6)) and (0.3-(0.05, 0.6)), respectively (Table 1 and Fig. 6).

Fig. 8 shows that model VM5b fits better than VM5a along the U.S. Atlantic coast (e.g. site Brig) and also in Laurentia. This is consistent with the finding of Engelhart *et al.* (2011). Meanwhile, our two laterally heterogeneous models (0.275-(0.05, 0.6) and 0.3-(0.05, 0.6)) can match the observed RSL data at the same level as VM5b. However, in the Fennoscandian region, VM5b cannot fit the data as well as these two laterally heterogeneous models (e.g. site Bell, Arnp, Leeu and Neub). Overall, these two laterally heterogeneous models fit better with the observed RSL data than the homogeneous model.

In summary, laterally heterogeneous models 0.3-(0.05, 0.6) and 0.275-(0.05, 0.6) can match the observed RSL data very well—not only in Fennoscandia but also globally. Moreover, they can explain the g-dot and u-dot data in Laurentia simultaneously. Unfortunately, their predicted g-dot and u-dot in Fennoscandia are still lower than the observed.

4.4 Fitting peak rates in Fennoscandia

In order to fit the observed g-dot and u-dot in Fennoscandia, the value of β_{UM} has been increased to 1 at 0.1 interval. Then we find that the present rates reach the largest value of 1.16 μGal yr^{-1} and 8.75 mm yr^{-1} when β_{UM} is around 0.5 [the model 0.3-(0.5, 0.6) in Table 1]. However, the predicted peak u-dot in Fennoscandia is still lower than the observed peak value. Moreover, the model with the largest present rates in Fennoscandia destroys the good fits we have achieved so far in Laurentia and in global RSL. Thus, unless we allow the β_{UM} value in Fennoscandia to be different from that in Laurentia, it is not possible to fit the observed global RSL data and peak g-dot and u-dot in Fennoscandia and Laurentia simultaneously.

To explore other options, we note that VM5a has a 40 km thick layer with viscosity equal to 1×10^{22} Pa s in the lower part of the lithosphere. It was incorporated to eliminate the misfit of surface motion in the region to the south of the Laurentide Ice Sheet (Peltier & Drummond 2008). Since the situation in Fennoscandia might be different, we have varied the viscosity of this thin layer to see if we can fit the observed data simultaneously. The results show that when the viscosity of this layer decreases to 1×10^{21} Pa s the largest g-dot and u-dot in Fennoscandia are 1.20 μGal yr^{-1} and 9.10 mm yr^{-1}, respectively [the model 0.3-(0.5, 0.6)-Fenno21 in Table 1]. However, this will also destroy the good fits in Laurentia and also the global RSL curves.

The remaining option is to modify the ice history in Fennoscandia and Barents Sea to eliminate the misfit in present day rates

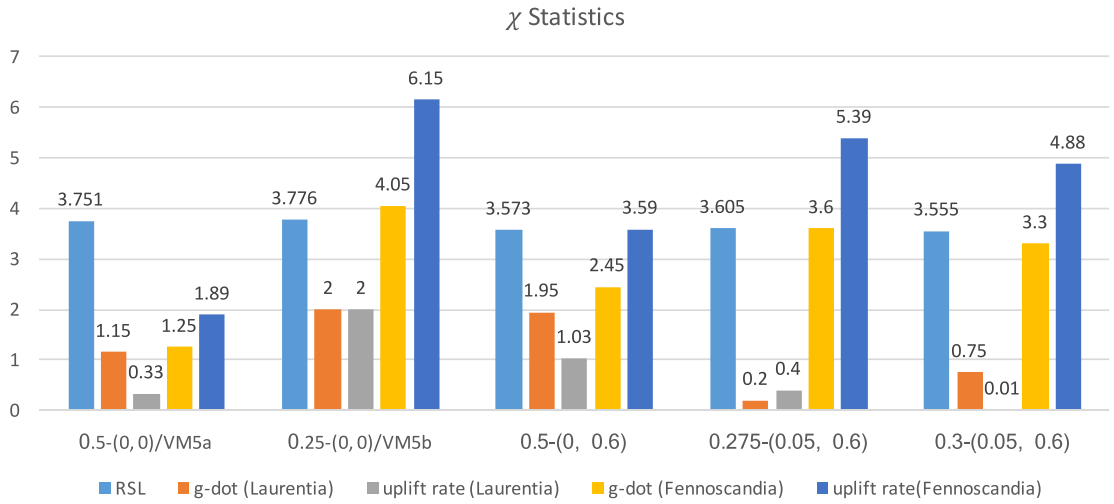

Figure 6. χ statistics of global RSL, g-dot and u-dot in Laurentia and Fennoscandia.

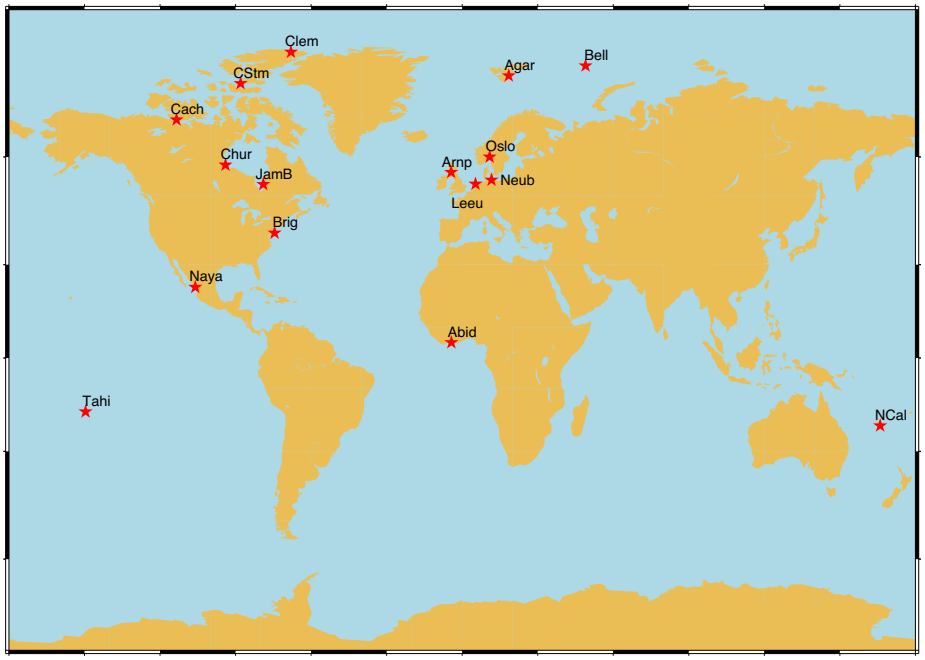

Figure 7. Locations of the 16 RSL sites shown in Fig. 8. Site abbreviation Abid is Abidjan, Ivory Coast, Agar is Agardhbukta Sval., Arnp is Arnprior, Bell is Bell Island FJL, Brig is Brigantine NJ., Cach is Cache Point - Lady Franklin Poin, Chur is Churchill, Man., Clem is Clem. Markham In., CStm is C. Storm Ell., JamB is James Bay, Que., Leeu is Leeuwarden Neth., Naya is Nayarit Mex., NCal is New Caledonia Fra., Neub is Neubukow, Oslo is Oslo Nor., Tahi is Tahiti.

there. It is well known that ICE-6G_C is much thicker than the ANU ice model (Lambeck 1995; Lambeck *et al.* 1998, 2010) in Fennoscandia especially during 18 to 14 kBP. However, a thinner ice in Fennoscandia would produce even lower g-dot and u-dot rates than predicted by ICE-6G_C, unless the viscosity in the lower mantle is allowed to increase. On the other hand, if we increase the ice thickness around the centre of Fennoscandia (where g-dot peaks) by about 50 per cent, the model with $\beta_{\rm UM} = 0.4$ in Fennoscandia and $\beta_{\rm UM} = 0.05$ everywhere else is able to predict g-dot and u-dot of 1.30 μGal yr^{-1} and 10.20 mm yr^{-1} respectively while the fit of the peak rates in Laurentia and global RSL only deteriorate slightly [the model 0.3-(0.4/0.05, 0.6)-ICE in Table 1]. However, the resulting ice profile might not be physically realistic. Another suggestion is that the ice thickness of ICE-6G_C in the Barents Sea might be overestimated (Auriac *et al.* 2016). Thus, its peripheral bulge might interfere with the uplift in Fennoscandia—resulting in a diminished g-dot and u-dot there.

5 CONCLUSION

As noted in Section 1, previous studies mostly focus on the effects of lateral heterogeneity or its sensitivity on GIA predictions. Very few works have addressed the important issue of whether lateral heterogeneity is the solution to solving the misfits between GIA predictions and observations. This paper attempts to fill this gap. Here, the ICE-6G_C model is used to search for the best laterally heterogeneous earth model that can fit the global sea level data, peak g-dot and u-dot in Laurentia and Fennoscandia simultaneously. Due to the limited scope of this paper, the background viscosity model is assumed to be similar to VM5a, although the viscosity in the upper

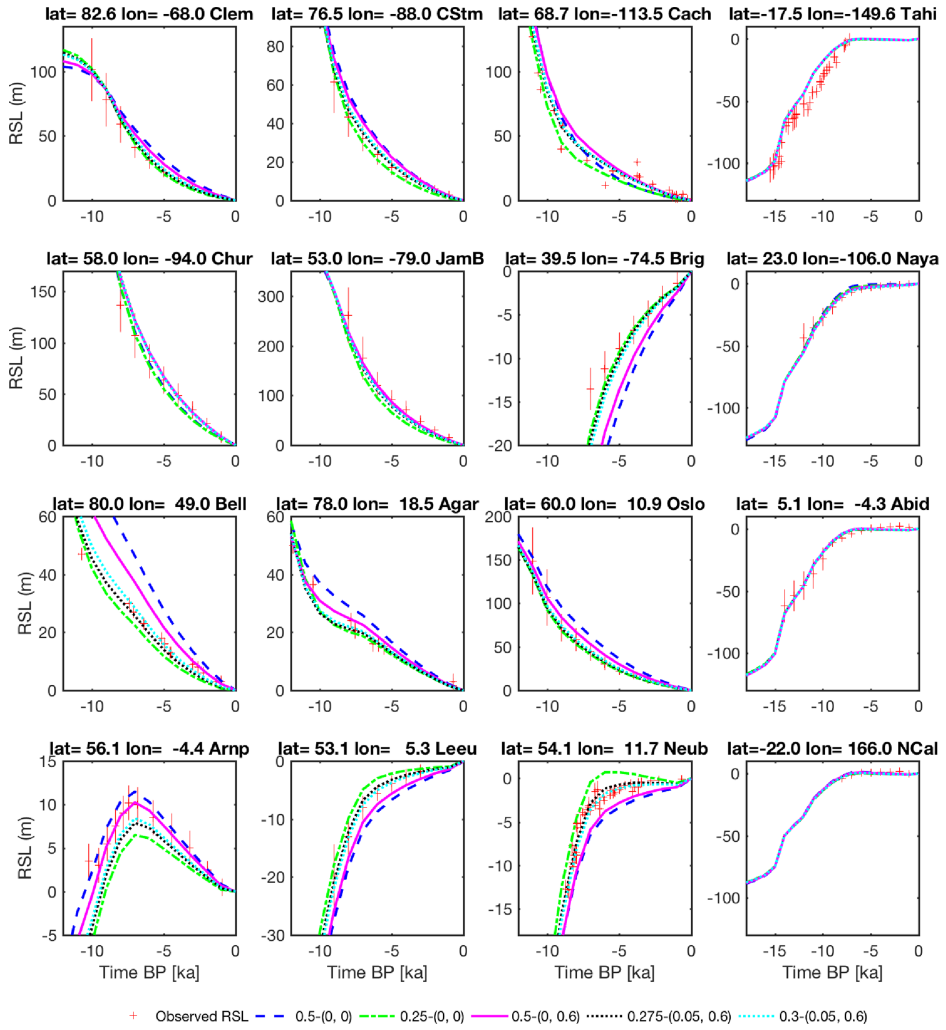

Figure 8. RSL curves at the 16 sites predicted by laterally homogeneous models and heterogeneous models (see the text) are compared with the observed data (with error bars).

Table 1. Comparison of model predictions versus observations of the global RSL data and the peak uplift rates of gravity (g-dot) and vertical deformation (u-dot) in Laurentia and Fennoscandia. Model naming follows X-(β_{UM}, β_{LM}) with X giving the upper-mantle background viscosity in 10^{21} Pa s, (β_{UM}, β_{LM}) represent the scaling factors to give lateral viscosity variations in the upper and lower mantle, respectively.

	Global	Laurentia		Fennoscandia	
Model	χ^{RSL}	g-dot (μGal yr^{-1})	u-dot (mm yr^{-1})	g-dot (μGal yr^{-1})	u-dot (mm yr^{-1})
0.5-(0, 0)/VM5a	3.751	1.97	12.68	1.05	7.97
0.25-(0,0)/VM5b	3.776	1.40	9.50	0.54	4.05
0.5-(0, 0.6)	3.573	2.19	14.05	0.86	6.61
0.3-(0.2, 0.6)	3.593	2.10	13.40	0.92	7.05
0.3-(0.1, 0.6)	3.600	1.96	12.65	0.78	5.97
0.3-(0.05, 0.6)	3.555	1.95	12.52	0.69	5.30
0.275-(0.2, 0.6)	3.592	2.06	13.25	0.86	6.64
0.275-(0.1, 0.6)	3.589	1.92	12.27	0.69	5.30
0.275-(0.05, 0.6)	3.605	1.84	11.90	0.63	4.81
0.25-(0.2, 0.6)	3.610	1.99	12.82	0.81	6.20
0.25-(0.1, 0.6)	3.652	1.82	11.77	0.64	4.93
0.25-(0.05, 0.6)	3.684	1.76	11.38	0.57	4.33
0.3-(0.5, 0.6)	4.036	2.31	14.30	1.16	8.75
0.3-(0.5, 0.6)-Fenno21	4.165	2.31	14.30	1.20	9.10
0.3-(0.4/0.05, 0.6)-ICE	3.651	1.94	12.48	1.30	10.20
Peak observed rates		1.8 ± 0.2	12.5 ± 1.5	1.35 ± 0.2	10.20 ± 1

mantle is allowed to vary. Lateral viscosity variations are assumed to be given by Bunge and Grand's seismic tomography model. The results can be summarized as follows:

(1) Starting with the background viscosity profile given by VM5a, the model that can best fit the global sea level data is found to have $\beta_{UM} = 0$ and β_{LM} around 0.6. However, this model, laterally homogeneous in the upper mantle, cannot match the peak g-dot and u-dot in Laurentia and Fennoscandia simultaneously.

(2) However, if the upper-mantle background viscosity is allowed to decrease, then two laterally heterogeneous models can be found to fit the global sea level data, peak g-dot and u-dot in Laurentia. Their upper-mantle background viscosities is 0.275×10^{21} or 0.3×10^{21} Pa s and they are consistent with the Fennoscandian relaxation spectrum result (Lau *et al.* 2016). However, the predicted g-dot and u-dot in the Fennoscandian area are still smaller than the observed values.

(3) To be able to fit the global sea level data, peak g-dot and u-dot in Laurentia and Fennoscandia simultaneously, either the value of β_{UM} in Northern Europe must be allowed to be different from that in Laurentia or the ice history in Fennoscandia and Barents Sea needs to be modified.

A rather surprising result of this study is the low value of β_{UM}, which implies that the contribution of thermal effects on seismic shear velocities is very low there. This is contrary to the observation that there is a good correlation between isotropic wave speed in the shallow upper mantle and surface tectonics with thermal origin. The problem is possibly due to the trade-off between the background viscosity and the value of β (see Fig. 5). Fig. 2(a) shows that the viscosity perturbations are positive under North America and Fennoscandia, so an increase in β_{UM} will result in a larger viscosity in the shallow upper mantle under these places. However, a similar effect can also be achieved under North America and Fennoscandia by making β_{UM} very small, but getting the background viscosity in the upper mantle high enough so that it is close to the radial average of the actual viscosity there. There may also be a trade-off between the value of β and the background viscosity in the lower mantle or in the sublithosphere. Thus, future studies should investigate such trade-off between the values of β and the background viscosity profile, in addition to the effects of different seismic tomography models and ice models. Nevertheless, we have shown that the introduction of lateral viscosity variations of a certain range of magnitude can help resolve some misfits in global RSL data, and can also fit the peak g-dot and u-dot in Laurentia simultaneously.

ACKNOWLEDGEMENTS

We are grateful to Dick Peltier for providing the ice model ICE-6G_C and for his constructive criticism of the manuscript and also for two reviewers for their comments. This work is supported by GRF grant 17315316 from the Hong Kong Research Grants Council to PW. HW is supported by the National Natural Science Foundation of China (Grant Nos. 41431070 and 41590854). The FE calculation was performed with the ABAQUS package from Hibbitt, Karlsson and Sorensen Inc. This research is conducted, in part, using the research computing facilities and/or advisory services offered by Information Technology Services, the University of Hong Kong.

REFERENCES

A, G., Wahr, J. & Zhong, S., 2012. Computations of the viscoelastic response of a 3-D compressible Earth to surface loading: an application to Glacial Isostatic Adjustment in Antarctica and Canada, *Geophys. J. Int.,* **192**(2), 557–572.

Argus, D. F., Peltier, W., Drummond, R. & Moore, A.W., 2014. The Antarctica component of postglacial rebound model ICE-6G_C (VM5a) based on GPS positioning, exposure age dating of ice thicknesses, and relative sea level histories, *Geophys. J. Int.,* **198**(1), 537–563.

Auriac, A., Whitehouse, P., Bentley, M., Patton, H., Lloyd, J. & Hubbard, A., 2016. Glacial isostatic adjustment associated with the Barents Sea ice sheet: a modelling inter-comparison, *Quat. Sci. Rev.,* **147,** 122–135.

Bunge, H.-P. & Grand, S.P., 2000. Mesozoic plate-motion history below the northeast Pacific Ocean from seismic images of the subducted Farallon slab, *Nature,* **405**(6784), 337–340.

Dyke, A., Andrews, J., Clark, P., England, J., Miller, G., Shaw, J. & Veillette, J., 2002. The Laurentide and Innuitian ice sheets during the last glacial maximum, *Quat. Sci. Rev.,* **21**(1), 9–31.

Ekström, G. & Dziewonski, A.M., 1998. The unique anisotropy of the Pacific upper mantle, *Nature,* **394**(6689), 168–172.

Engelhart, S., Peltier, W. & Horton, B., 2011. Holocene relative sea-level changes and glacial isostatic adjustment of the US Atlantic coast, *Geology,* **39**(8), 751–754.

Gasperini, P. & Sabadini, R., 1989. Lateral heterogeneities in mantle viscosity and post-glacial rebound, *Geophys. J. Int.,* **98**(3), 413–428.

Gasperini, P., Sabadini, R. & Yuen, D., 1991. Deep continental roots: the effects of lateral variations of viscosity on post-glacial rebound, in *Glacial Isostasy, Sea-Level and Mantle Rheology,* pp. 21–32, eds Sabadini, R., Lambeck, K. & Boschi, E. Springer.

Giunchi, C., Spada, G. & Sabadini, R., 1997. Lateral viscosity variations and post-glacial rebound: effects on present-day VLBI baseline deformations, *Geophys. Res. Lett.,* **24**(1), 13–16.

Hawkes, A.D. *et al.*, 2016. Relative sea-level change in northeastern Florida (USA) during the last 8.0 ka, *Quat. Sci. Rev.,* **142,** 90–101.

Ivins, E.R. & Sammis, C.G., 1995. On lateral viscosity contrast in the mantle and the rheology of low-frequency geodynamics, *Geophys. J. Int.,* **123**(2), 305–322.

Karato, S., 2008. *Deformation of Earth Materials. An Introduction to the Rheology of Earth Materials,* Cambridge Univ. Press.

Kaufmann, G. & Lambeck, K., 2000. Mantle dynamics, postglacial rebound and the radial viscosity profile, *Phys. Earth planet. Inter.,* **121**(3), 301–324.

Kaufmann, G. & Wolf, D., 1996. Deglacial land emergence and lateral upper-mantle heterogeneity in the Svalbard Archipelago—II. Extended results for high-resolution load models, *Geophys. J. Int.,* **127**(1), 125–140.

Kaufmann, G. & Wu, P., 1998. Lateral asthenospheric viscosity variations and postglacial rebound: a case study for the Barents Sea, *Geophys. Res. Lett.,* **25**(11), 1963–1966.

Kaufmann, G. & Wu, P., 2002. Glacial isostatic adjustment in Fennoscandia with a three-dimensional viscosity structure as an inverse problem, *Earth planet. Sci. Lett.,* **197**(1-2), 1–10.

Kaufmann, G., Wu, P. & Wolf, D., 1997. Some effects of lateral heterogeneities in the upper mantle on postglacial land uplift close to continental margins, *Geophys. J. Int.,* **128**(1), 175–187.

Kaufmann, G., Wu, P. & Li, G., 2000. Glacial isostatic adjustment in Fennoscandia for a laterally heterogeneous earth, *Geophys. J. Int.,* **143**(1), 262–273.

Kaufmann, G., Wu, P. & Ivins, E.R., 2005. Lateral viscosity variations beneath Antarctica and their implications on regional rebound motions and seismotectonics, *J. Geodyn.,* **39**(2), 165–181.

Kierulf, H.P., Steffen, H., Simpson, M.J.R., Lidberg, M., Wu, P. & Wang, H., 2014. A GPS velocity field for Fennoscandia and a consistent comparison to glacial isostatic adjustment models, *J. geophys. Res.,* **119**(8), 6613–6629.

Lambeck, K., 1995. Late Devensian and Holocene shorelines of the British Isles and North Sea from models of glacio-hydro-isostatic rebound, *J. Geol. Soc.,* **152**(3), 437–448.

Lambeck, K. & Johnston, P., 1998. The viscosity of the mantle: evidence from analyses of glacial rebound phenomena, in *The Earth's Mantle: Composition, Structure, and Evolution,* pp. 461–502, ed. Jackson, I., Cambridge Univ. Press.

Lambeck, K., Smither, C. & Johnston, P., 1998. Sea-level change, glacial rebound and mantle viscosity for northern Europe, *Geophys. J. Int.,* **134**(1), 102–144.

Lambeck, K., Purcell, A., Zhao, J. & Svensson, N.-O., 2010. The Scandinavian ice sheet: from MIS 4 to the end of the Last Glacial Maximum, *Boreas,* **39**(2), 410–435.

Lambeck, K., Rouby, H., Purcell, A., Sun, Y. & Sambridge, M., 2014. Sea level and global ice volumes from the Last Glacial Maximum to the Holocene, *Proc. Natl. Acad. Sci. USA,* **111**(43), 15 296–15 303.

Lambert, A., Henton, J., Mazzotti, S., James, T., Courtier, N., Huang, J. & Van Der Kamp, G., 2013. Postglacial rebound and total water storage variations in the Nelson River drainage basin: a gravity GPS Study. Open File, Geol. Surv. Canada, 7317.

Latychev, K., Mitrovica, J.X., Tamisiea, M.E., Tromp, J. & Moucha, R., 2005a. Influence of lithospheric thickness variations on 3-D crustal velocities due to glacial isostatic adjustment, *Geophys. Res. Lett.,* **32**(1), doi:10.1029/2004GL021454.

Latychev, K., Mitrovica, J.X., Tromp, J., Tamisiea, M.E., Komatitsch, D. & Christara, C.C., 2005b. Glacial isostatic adjustment on 3-D Earth models: a finite-volume formulation, *Geophys. J. Int.,* **161**(2), 421–444.

Lau, H.C., Mitrovica, J.X., Austermann, J., Crawford, O., Al-Attar, D. & Latychev, K., 2016. Inferences of mantle viscosity based on ice age data sets: radial structure, *J. geophys. Res.,* **121**(10), 6991–7012.

Martinec, Z. & Wolf, D., 2005. Inverting the Fennoscandian relaxation-time spectrum in terms of an axisymmetric viscosity distribution with a lithospheric root, *J. Geodyn.,* **39**(2), 143–163.

Mitrovica, J.X. & Forte, A.M., 1997. Radial profile of mantle viscosity: results from the joint inversion of convection and postglacial rebound observables, *J. geophys. Res.,* **102**(B2), 2751–2769.

Olsson, P.-A., Milne, G., Scherneck, H.-G. & Ågren, J., 2015. The relation between gravity rate of change and vertical displacement in previously glaciated areas, *J. Geodyn.,* **83,** 76–84.

Paulson, A., Zhong, S. & Wahr, J., 2005. Modelling post-glacial rebound with lateral viscosity variations, *Geophys. J. Int.,* **163**(1), 357–371.

Peltier, W., 1998. Postglacial variations in the level of the sea: implications for climate dynamics and solid-earth geophysics, *Rev. Geophys.,* **36**(4), 603–689.

Peltier, W., 2004. Global glacial isostasy and the surface of the ice-age Earth: the ICE-5G (VM2) model and GRACE, *Annu. Rev. Earth planet. Sci.,* **32,** 111–149.

Peltier, W. & Drummond, R., 2008. Rheological stratification of the lithosphere: a direct inference based upon the geodetically observed pattern of the glacial isostatic adjustment of the North American continent, *Geophys. Res. Lett.,* **35,** doi:10.1029/2008GL034586 .

Peltier, W., Argus, D. & Drummond, R., 2015. Space geodesy constrains ice age terminal deglaciation: the global ICE-6G_C (VM5a) model, *J. geophys. Res.,* **120**(1), 450–487.

Roy, K. & Peltier, W., 2015. Glacial isostatic adjustment, relative sea level history and mantle viscosity: reconciling relative sea level model predictions for the US East coast with geological constraints, *Geophys. J. Int.,* **201**(2), 1156–1181.

Sabadini, R. & Gasperini, P., 1989. Glacial isostasy and the interplay between upper and lower mantle lateral viscosity heterogeneities, *Geophys. Res. Lett.,* **16**(5), 429–432.

Sabadini, R., Yuen, D.A. & Portney, M., 1986. The effects of upper-mantle lateral heterogeneities on postglacial rebound, *Geophys. Res. Lett.,* **13**(4), 337–340.

Schotman, H., Wu, P. & Vermeersen, L., 2008. Regional perturbations in a global background model of glacial isostasy, *Phys. Earth planet. Inter.,* **171**(1-4), 323–335.

Schotman, H., Vermeersen, L., Wu, P., Drury, M. & De Bresser, J., 2009. Constraints on shallow low-viscosity zones in Northern Europe from future GOCE gravity data, *Geophys. J. Int.,* **178**(1), 65–84.

Simon, K., James, T., Henton, J. & Dyke, A., 2016. A glacial isostatic adjustment model for the central and northern Laurentide Ice Sheet based on relative sea level and GPS measurements, *Geophys. J. Int.,* **205**(3), 1618–1636.

Spada, G., Antonioli, A., Cianetti, S. & Giunchi, C., 2006. Glacial isostatic adjustment and relative sea-level changes: the role of lithospheric and upper mantle heterogeneities in a 3-D spherical earth, *Geophys. J. Int.,* **165**(2), 692–702.

Steffen, H. & Wu, P., 2014. The sensitivity of GNSS measurements in Fennoscandia to distinct three-dimensional upper-mantle structures, *Solid Earth,* **5**(1), 557, doi: 10.5194/se-5-557-2014.

Steffen, H., Kaufmann, G. & Wu, P., 2006. Three-dimensional finite-element modeling of the glacial isostatic adjustment in Fennoscandia, *Earth planet. Sci. Lett.,* **250**(1-2), 358–375.

Steffen, H., Wu, P. & Kaufmann, G., 2007. Sensitivity of crustal velocities in Fennoscandia to radial and lateral viscosity variations in the mantle, *Earth planet. Sci. Lett.,* **257**(3-4), 474–485.

Steffen, H., Wu, P. & Wang, H., 2012. Optimal locations for absolute gravity measurements and sensitivity of GRACE observations for constraining glacial isostatic adjustment on the northern hemisphere, *Geophys. J. Int.,* **190**(3), 1483–1494.

Steffen, H., Kaufmann, G. & Lampe, R., 2014a. Lithosphere and upper-mantle structure of the southern Baltic Sea estimated from modelling relative sea-level data with glacial isostatic adjustment, *Solid Earth,* **5**(1), 447–459.

Steffen, H., Wu, P. & Wang, H., 2014b. Optimal locations of sea-level indicators in glacial isostatic adjustment investigations, *Solid Earth,* **5**(1), 511–521.

Tanaka, Y., Klemann, V., Martinec, Z. & Riva, R., 2011. Spectral-finite element approach to viscoelastic relaxation in a spherical compressible earth: application to GIA modelling, *Geophys. J. Int.,* **184**(1), 220–234.

Wahr, J., Dazhong, H. & Trupin, A., 1995. Predictions of vertical uplift caused by changing polar ice volumes on a viscoelastic Earth, *Geophys. Res. Lett.,* **22**(8), 977–980.

Wang, H. & Wu, P., 2006a. Effects of lateral variations in lithospheric thickness and mantle viscosity on glacially induced relative sea levels and long wavelength gravity field in a spherical, self-gravitating Maxwell Earth, *Earth planet. Sci. Lett.,* **249**(3), 368–383.

Wang, H. & Wu, P., 2006b. Effects of lateral variations in lithospheric thickness and mantle viscosity on glacially induced surface motion on a spherical, self-gravitating Maxwell Earth, *Earth planet. Sci. Lett.,* **244**(3), 576–589.

Wang, H. & Wu, P., 2006c. Role of background viscosity in the investigation of postglacial rebound induced crustal motion in a laterally heterogeneous mantle, *J. Geodyn.,* **42**(1), 85–94.

Wang, H., Wu, P. & van der Wal, W., 2008. Using postglacial sea level, crustal velocities and gravity-rate-of-change to constrain the influence of thermal effects on mantle lateral heterogeneities, *J. Geodyn.,* **46**(3-5), 104–117.

Wang, H., Wu, P., Jia, L., Hu, B. & Jiang, L., 2011. The role of glacial isostatic adjustment in the present-day crustal motion and sea levels of East Asia, *Earth Planets Space,* **63**(8), 915–928.

Wang, H. *et al.*, 2013. Increased water storage in North America and Scandinavia from GRACE gravity data, *Nat. Geosci.,* **6**(1), 38–42.

Wang, H., Xiang, L., Jia, L., Wu, P., Steffen, H., Jiang, L. & Shen, Q., 2015. Water storage changes in North America retrieved from GRACE gravity and GPS data, *Geod. Geodyn.,* **6**(4), 267–273.

Whitehouse, P., Latychev, K., Milne, G.A., Mitrovica, J.X. & Kendall, R., 2006. Impact of 3-D earth structure on Fennoscandian glacial isostatic adjustment: implications for space-geodetic estimates of present-day crustal deformations, *Geophys. Res. Lett.,* **33**(13), doi:10.1029/2006GL026568.

Wu, P., 2002. Mode coupling in a viscoelastic self-gravitating spherical earth induced by axisymmetric loads and lateral viscosity variations, *Earth planet. Sci. Lett.,* **202**(1), 49–60.

Wu, P., 2004. Using commercial finite element packages for the study of earth deformations, sea levels and the state of stress, *Geophys. J. Int.,* **158**(2), 401–408.

Wu, P., 2005. Effects of lateral variations in lithospheric thickness and mantle viscosity on glacially induced surface motion in Laurentia, *Earth planet. Sci. Lett.,* **235**(3-4), 549–563.

Wu, P., 2006. Sensitivity of relative sea levels and crustal velocities in Laurentide to radial and lateral viscosity variations in the mantle, *Geophys. J. Int.,* **165**(2), 401–413.

Wu, P. & van der Wal, W., 2003. Postglacial sealevels on a spherical, self-gravitating viscoelastic earth: effects of lateral viscosity variations in the upper mantle on the inference of viscosity contrasts in the lower mantle, *Earth planet. Sci. Lett.,* **211**(1–2), 57–68.

Wu, P., Wang, H. & Schotman, H., 2005. Postglacial induced surface motions, sea-levels and geoid rates on a spherical, self-gravitating laterally heterogeneous earth, *J. Geodyn.,* **39**(2), 127–142.

Wu, P., Steffen, H. & Wang, H., 2010. Optimal locations for GPS measurements in North America and Northern Europe for constraining glacial isostatic adjustment, *Geophys. J. Int.,* **181**(2), 653–664.

Wu, P., Wang, H. & Steffen, H., 2013. The role of thermal effect on mantle seismic anomalies under Laurentia and Fennoscandia from observations of glacial isostatic adjustment, *Geophys. J. Int.,* **192**(1), 7–17.

Zhong, S., Paulson, A. & Wahr, J., 2003. Three-dimensional finite-element modelling of Earth's viscoelastic deformation: effects of lateral variations in lithospheric thickness, *Geophys. J. Int.,* **155**(2), 679–695.

APPENDIX A: SENSITIVITY ANALYSIS

For the interpretation of the results in this paper, it is useful to understand the sensitivity of these three types of data (RSL, g-dot and u-dot) to lateral viscosity variations. The sensitivity kernel for a laterally heterogeneous Earth can be obtained from the approach of Wu (2006) and Steffen *et al.* (2012, 2014b), who showed that the sensitivity kernel for RSL does depend on time. However, Wu *et al.* (2013) only showed the normalized sensitivity for u-dot and g-dot at the present time, which is also applicable for RSL during the last 6 kBP. So we want to show the sensitivity kernel for RSL at earlier times and see how it evolves with time here.

The sensitivity of a certain measurement to a specific model parameter is obtained from the difference between the predictions of two models which only differ in that parameter (Wu 2006; Steffen *et al.* 2012). In this paper, we compute the g-dot and u-dot sensitivity to lateral heterogeneity of upper and lower mantle (Fig. A1). Also, we calculate the RSL sensitivity to lateral heterogeneity of upper and lower mantle at different times (Fig. A2). In these plots, we use the actual value of the sensitivity rather than the normalized absolute values as in Wu *et al.* (2013).

Fig. A1 shows that both g-dot and u-dot in Laurentia, Fennoscandia, Greenland and part of Antarctica are sensitive to lateral heterogeneities in the upper mantle, but only g-dot and u-dot around the centre of the ancient Laurentian ice sheet have the highest sensitivity to lower-mantle lateral heterogeneity. These findings are consistent with that in Wu *et al.* (2013) because how deep the ice can 'see' mainly depends on the lateral dimension of the ice sheet—only the ice sheet in Laurentia is large enough to 'see' deep into the lower mantle.

As for the RSL sensitivity in the upper mantle, Figs A2(a), (c), (e) and (g) show that large positive values are concentrated northwest of Norway and between Canada and Greenland, while large negative values are found in the Barents Sea, centre of Fennoscandia and around Hudson Bay. Note that both the coverage and their magnitudes diminish with time, from −270 and 170 m at 18 kBP to −25 and 30 m at 4 kBP. However, the location of these centres does not change with time except for the one located at the west of Hudson Bay which moves slightly northeastwards towards Hudson Bay before 10 kBP.

As for the RSL sensitivity in the lower mantle (see Figs A2 b,d, f and h), the magnitudes are much smaller and decrease from −44 and 16 m at 18 kBP to −6 and 14 m at 4 kBP. So the large negative amplitude in the East Siberian Sea and the smaller negative ones around the Barents Sea, Fennoscandia, British Isles and Greenland become very small and almost vanish completely from the map after about 4 kBP. Near central Canada, the amplitude of sensitivity decreases to 10 m at 12 kBP, then the two positive peaks that appear southwest of this centre move northeastwards and grow into one large peak at 7 kBP. After that, this positive peak diminishes to about 5 m after 2 kBP.

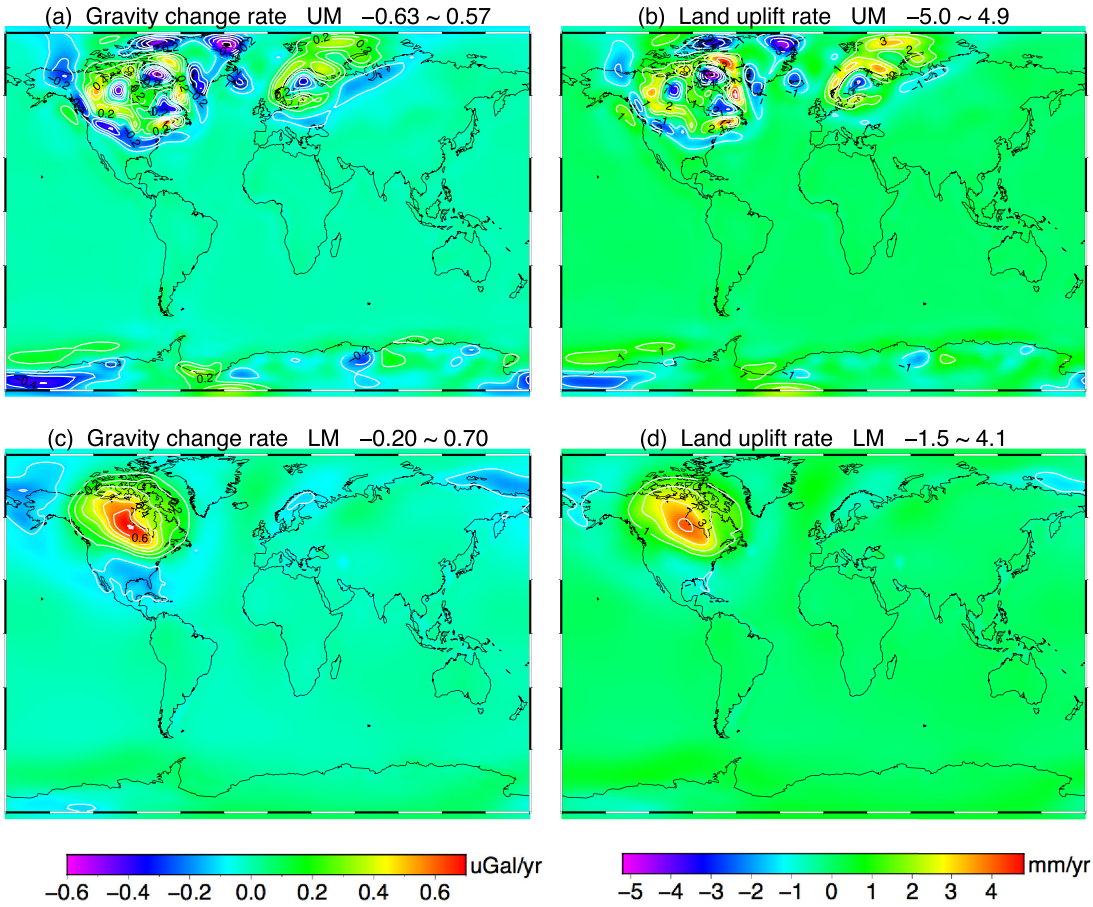

Figure A1. Sensitivity of g-dot to lateral heterogeneity in the (a) upper mantle and (c) lower mantle; u-dot to lateral heterogeneity in the (b) upper mantle and (d) lower mantle.

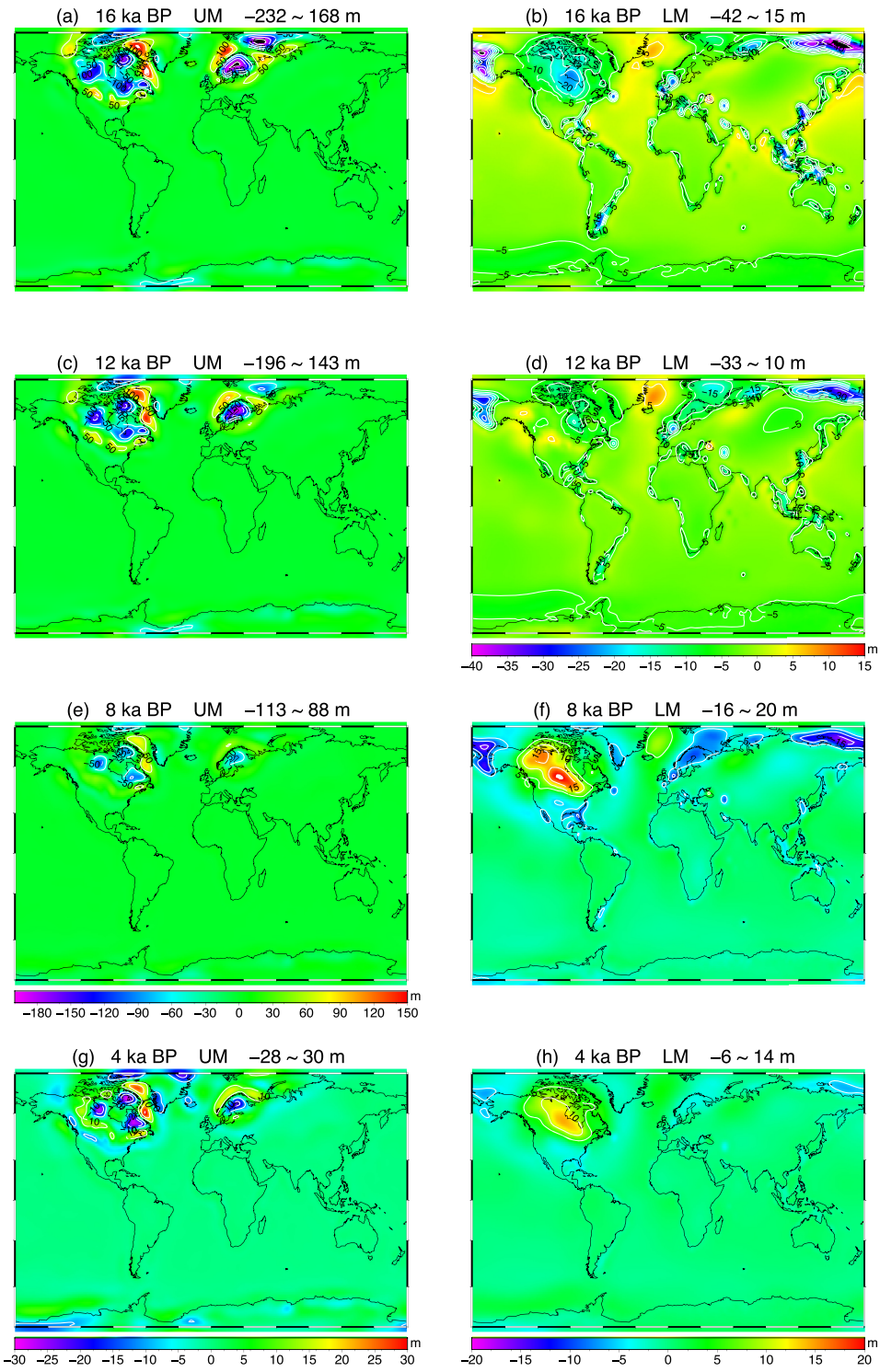

Figure A2. Sensitivity of RSL to lateral heterogeneity of upper mantle at (a) 16, (c) 12, (e) 8 and (g) 4 ka, and lower mantle at (b) 16, (d) 12, (f) 8 and (h) 4 ka before present. The minimum and maximum values are also given above each map. Note that (a), (c) and (e) share the same colour bar, (b) and (d) share the same colour bar, and (f) and (h) share the same colour bar.

APPENDIX B: EFFECT OF TOMOGRAPHY MODEL S20A

In this appendix, we would like to see if the results of Figs 3 and 4 are dependent on the choice of the seismic tomography model. So we repeat the computations of Figs 3 and 4 using viscosity models converted from the seismic tomography model S20A (Ekström & Dziewonski 1998) instead of Bunge and Grand's model. The results are shown in Fig. B1. Here we do not include the time-dependent coastline. The value for the RSL χ statistics increases with the increase of β_{UM}, just like the pattern in Fig. 3. Also, the best solution also has β_{UM} around 0 and β_{LM} around 0.6. Furthermore, the predicted peak values of g-dot and u-dot in Laurentia and Fennoscandia follow the same change pattern as we illustrate in Fig. 4. Therefore, the results in Figs 3 and 4 are not dependent on the choice of Bunge and Grand's seismic tomography model.

Clearly, this statement is far from definitive and more seismic tomography models need to be investigated before a firm conclusion can be reached.

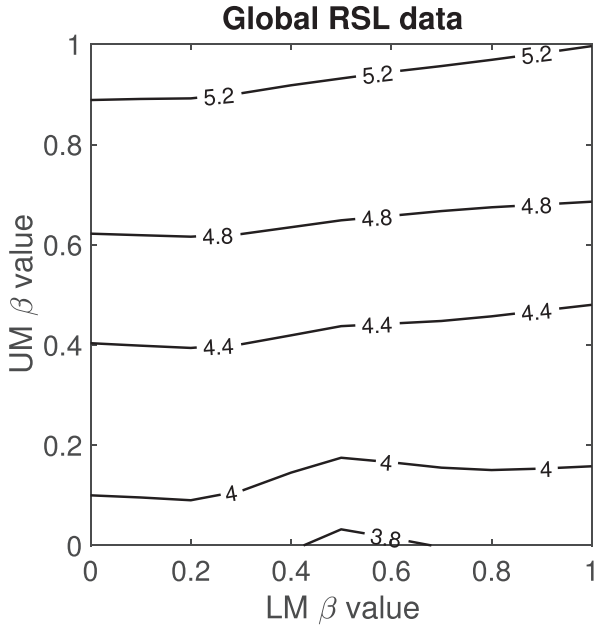

Figure B1. Contour plots of χ for model ICE-6G_C (VM5a) paired with S20A tomography model when all 262 RSL sites are used.

APPENDIX C: COMPARISON OF THE BACKGROUND VISCOSITY MODELS MENTIONED IN THIS PAPER

Table C1 compares the background viscosity models of VM5a, VM5b and that for our best laterally heterogeneous models. They only differ in the viscosity of the upper mantle between 100 and 670 km depth.

Table C1. Comparison of the background viscosity models mentioned in the paper.

Depth range\models (km)	VM5a ($\times 10^{21}$ Pa s)	VM5b ($\times 10^{21}$ Pa s)	Best laterally heterogeneous models ($\times 10^{21}$ Pa s)
0–60	Elastic	Elastic	Elastic
60–100	10.0	10.0	10.0
100–420	0.50	0.25	0.275–0.3
420–670	0.50	0.25	0.275–0.3
670–1260	1.57	1.57	1.57
1260–2890	3.23	3.23	3.23